*Type of the Paper (Article)*

# Identification of potent inhibitors against Aurora kinase A using molecular docking and molecular dynamics simulation studies

**Sathishkumar Chinnasamy[1#], Gurudeeban Selvaraj[2,3,6#], Aman Chandra Kaushik[1], Satyavani Kaliamurthi[2,3,6], Asma Sindhoo Nangraj[1], Chandrabose Selvaraj[4], Sanjeev Kumar Singh[4], Ramanathan Thirugnanasambandam[5], Keren Gu[2,6], Dong-Qing Wei[1,2,3*]**

[1]The State Key Laboratory of Microbial Metabolism, College of Life Sciences and Biotechnology, Shanghai Jiao Tong University, No: 800 Dongchuan Road, Minhang, Shanghai, 200240, China; sathishimb@sjtu.edu.cn or sathishimb@gmail.com (S.C.); amanbioinfo@gmail.com (A.C.K); sindhoo_sind@yahoo.com (A.S.N.); dqwei@sjtu.edu.cn (D.Q.W).

[2]Center of Interdisciplinary Science-Computational Life Sciences, College of Food Science and Engineering, Henan University of Technology, Zhengzhou High-tech Industrial Development Zone, Zone, 100 Lianhua Street, Zhengzhou, Henan 450001, China; satyavani.mkk@haut.edu.cn (S.K.); gurudeeb99@haut.edu.cn (G.S.); gkr@haut.edu.cn (K.G.).

[3]Peng Cheng Laboratory, Vanke Cloud City Phase I Building 8, Xili Street, Nanshan District, Shenzhen, Guangdong, 518055, China

[4]Department of Bioinformatics, School of Biological Sciences, Alagappa University, Karaikkudi 630004, Tamil Nadu, India; selnikraj@gmail.com (C.S); skysanjeev@gmail.com (S.K.S),

[5]Centre of Advanced Study in Marine Biology, Faculty of Marine Science, Annamalai University, Parangipettai 608502, Tamil Nadu, India; drtramanathan@gmail.com

[6]College of Chemistry, Chemical Engineering and Environment, Henan University of Technology, Zhengzhou High-tech Industrial Development Zone, 100 Lianhua Street, Zhengzhou, Henan 450001, China.

[#] Authors equally contributed

***Corresponding Author:** Prof. Dong-Qing Wei, Department of Bioinformatics, The State Key Laboratory of Microbial Metabolism, College of Life Sciences and Biotechnology, Shanghai Jiao Tong Tong University, No: 800 Dongchuan Road, Minhang, Shanghai, 200240, China, Email: dqwei@sjtu.edu.cn (D.Q.W); Tel.: +86 021 3420 4717; Fax: +86 021 3420 5709

**Abstract:** Aurora kinase A (AURKA) is a normal cell proliferation-inducing enzyme encoded by AURKA gene, with over-expression observed in different types of malignancies. Hence, the goal is to find potential inhibitors against AURKA. In this study, molecular docking, Standard Precision and Extra Precision methods were employed. After the docking study, the ligands showed an extremely low binding score which suggested very high binding affinity of the ligands. Furthermore, Quantum polarized ligand docking (QPLD) was performed to predict the binding status of the molecules. Based on the binding affinity, the top four compounds were chosen for further analysis. The docked complexes were further analyzed in explicit water conditions using 100 ns molecular dynamics simulations and binding free energy calculation. Then, density functional theory (DFT) calculation was used to calculate the molecular properties of the molecules. Finally, systems biology experiments validated the molecular docking and molecular dynamics simulation studies and indicated that *quercetin, kaempferol, luteolin* and *rutin* could inhibit the AURKA. The results show that, these four molecules have high binding affinity to the AURKA and significant interactions (LEU139, GLU211and ALA213) were also identified with the hinge region of Aurora kinase A. Thus, LEU139, GLU211, and ALA213 were identified as the crucial protein mechanisms.

**Keywords:** Aurora kinase A, Molecular Docking, DFT, MD simulation.

## 1. Introduction

Aurora kinase (AURK) is a normal cell proliferation-inducing enzyme encoded by AURK gene in humans. It belongs to the family of serine/threonine kinase [1]. Based on its function, AURK is divided into three classes: AURKA, AURKB, and AURKC, which have almost similar ATP binding sites. AURKA essentially promotes mitotic entry, nucleation, centrosome separation, microtubule, spindle assembly, and development of microtubules, cytokinesis, and mitosis exit [1,2]. [1,2]. It plays an essential role in microtubule-kinetochore attachment, chromosome condensation, chromosomal segregation, cytokinesis regulation and chromosomal alignment [1,3]. AURKC promotes meiotic chromosome segregation, however, the detailed function is not known. Earlier studies report that the aberrant expression of AURKA and AURKB was observed in different types of malignancies. Overexpression of AURKA with hyperactivation of Wnt/Ras-MAPK signaling pathway causes colorectal cancer [4]. The drug resistance and tumorigenesis of AURK-A/B causes a higher prevalence of lung adenocarcinoma [5], refractory neuroblastoma [6], human papillomaviruses positive head/neck cancer [7], gastric cancer [8], and breast cancer [9,10]. In addition, AURKA have been identified as an important prognostic marker in lung adenocarcinoma from microarray meta-analysis [11]. The consequences of the existence of AURK in various cancers have led to the selection of AURKA as the target for cancer chemotherapy [1,12]. More than 10 AURK inhibitors were entered in the clinical trials, which included AMG-900 (Phase I), ENMD-2076, ENMD-2076, Alisertib, and danusertib hydrochloride (Phase II) [13-16]. The multicenter phase II study of different tumors using danusertib AURK inhibitors showed only an insignificant anti-tumor effect after unfortunate implications of systemic therapy [16]. Falchook and colleagues [17] reviewed the clinical impacts of the various AURKA, AURKB, and pan-AURK inhibitors and their AURK targets. The significant side effects of AURK inhibitors include febrile neutropenia, stomatitis inflammation, gastrointestinal disorders, and high blood pressure. A number of

 doi:10.20944/preprints201908.0238.v1



researches to find nontoxic drug candidates without adverse side effects in the treatment of AURK-mediated carcinogenesis are ongoing.

With this view, we have selected phytochemicals from plants, especially mangroves. A total of 148 phytochemicals, including alkaloids, flavonoids, phenolic compounds, volatile compounds, and their derivatives were identified using liquid chromatography coupled with mass-spectroscopy [18,19], gas-chromatography coupled with mass-spectroscopy [20], and reverse phase high-performance liquid-chromatographic [21,22,23] techniques from different mangroves (Supporting Information, Table S1). Studies report that these phytochemicals demonstrate different therapeutic effects, such as antimicrobial and antioxidants [24] and anti-nociceptive [25], antidiabetic [19,26], anticancer [27], wound-healing properties [28,29], having elastase, and collagenase [30], cyclooxygenase 2 [31], dipeptidyl peptidase-4 [32], PPAR-γ [33] and alpha-ketoglutarate dependent dioxygenase FTO inhibitory action [34]. Currently available aurora inhibitors namely ZM447439, Hesperadin, and VX-680 possess some side effects like alopecia, anemia, dry skin and toxicity on the bone marrow [35,36]. Therefore, there is an emerging need to find potent aurora inhibitors with low toxicity. Accordingly, we aimed to identify new AURKA inhibitors from plants based small molecules using various computational techniques such as molecular docking, quantum polarized ligand docking, molecular dynamics simulation, binding free energy calculation, and density functional theory calculation. Finally, these four compounds were validated by system biology approach. The molecular docking was used to calculate the binding energy, which is vital to interpret the biological activity of the ligands. Molecular dynamics simulation was used to monitor and evaluate the conformational behaviors of the atoms and molecules, which validate the outcomes of the molecular docking. The Prime MM-GBSA calculation is used to predict the binding free energy for a receptor and ligands. The DFT calculation evaluates the molecular properties such as electron density, molecular electrostatic map, and frontier molecular orbital density fields (eg. LUMO and HOMO). Systems biology is an interdisciplinary field of study that focuses on employing mathematical and computational modeling to acquire knowledge on complex biological organizations. There exists several strategies to investigate biological processes with the help of molecular interaction networks. Protein–protein interaction (PPI) data is often engaged to build networks, in which proteins are revealed to be interacting with functionally related partners. This leads to the budding of functionally related sub-networks referred to as “functional modules”. Modular organization of function occurs across species, and knowledge about gene function is important. Analogous networks have also been constructed using co-expression data, genetic interaction data, and data type combinations. Nevertheless, a limitation is that these networks consist of false positive and false negative interactions, which may misrepresent functional organizations.

 doi:10.20944/preprints201908.0238.v1



## 2. Results

The computational approaches of molecular docking, DFT, QPLD, binding free energy calculation, and MD simulations were employed. The approach used in the present study is presented as a workflow in Figure 1.

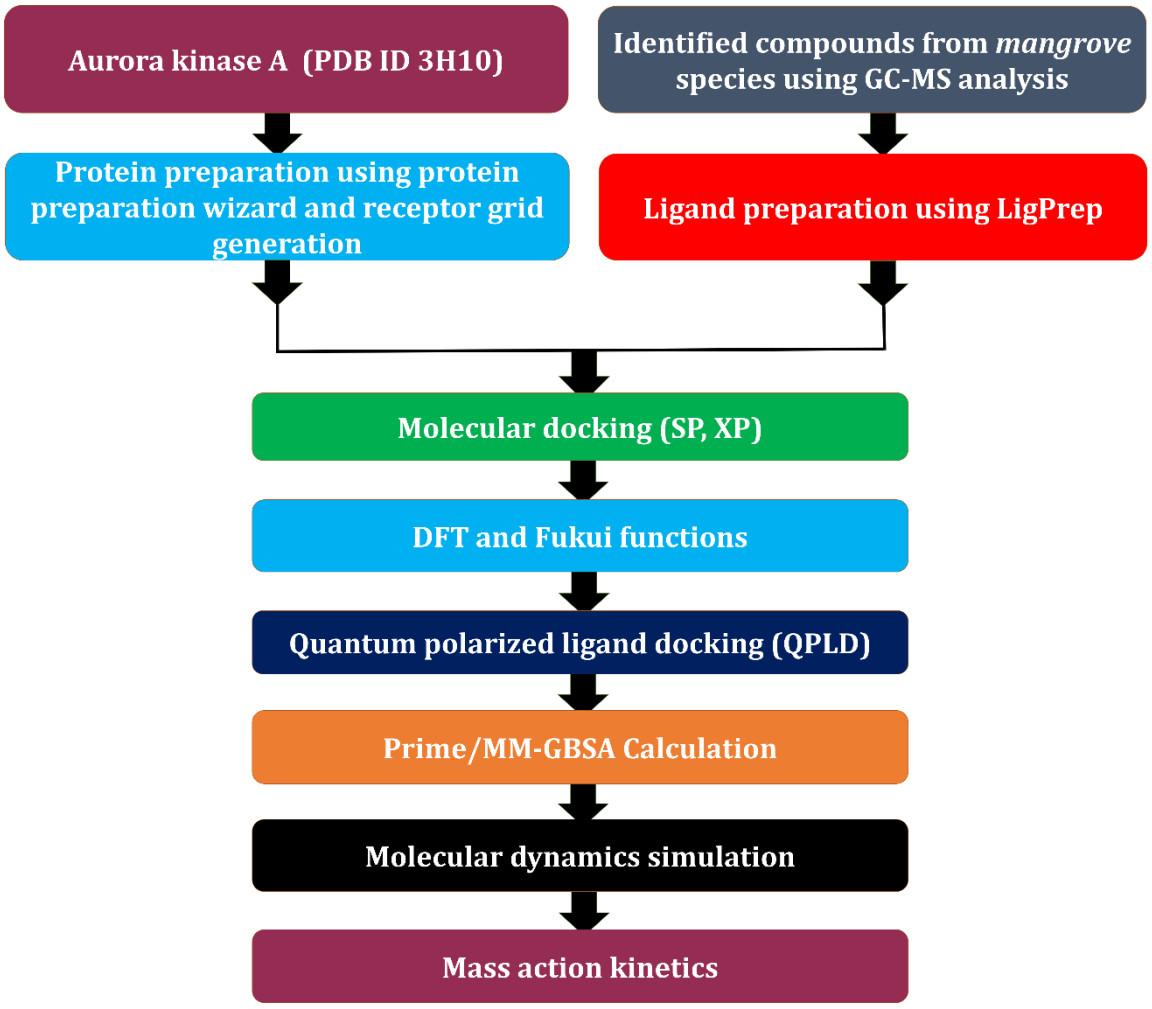


**Figure 1.** Flow chart depicting the methodology employed in the present study.

### *2.1. Active site prediction and molecular docking*

The crystal structure of Aurora kinase A was obtained from protein databank (http://www.rcsb.org) with accession ID 3H10. The molecular docking study was performed by Glide XP (Schrödinger Release 2018-3: Glide, Schrödinger, LLC, New York, NY, 2018). The identified identified compounds were used in our previous study [18-34]. These compounds were docked into the active site of AURKA. All the compounds were prioritized depending on the docking score (Supporting Information, Table S2). The most promising compounds with structural diversities and

 doi:10.20944/preprints201908.0238.v1



binding mode were taken on the basis of hydrogen bonding interactions and docking score. Finally, the top four compounds were chosen for further analysis. Figure 2 shows the protein ligand complexes with hydrogen bond interactions. These four inhibitors can develop H bonds with the GLU211 and ALA213 in the hinge region of the Aurora A (Figure 2). In the residues of 210–216 are the hinge region of Aurora kinase A, which plays a significant role in creating the catalytic active site site [37]. The active site residues of Aurora kinase A were fashioned by following the key residues LEU139, GLU211, and ALA213 [37]. These four inhibitors interacted with direct H-bonding network network with the main chain of AURKA, particularly the amino acid residues of LEU139, GLU211, and ALA213. Figure 2 shows that the inhibitors were binding to the active site pocket of Aurora kinase A via the H-bond interactions and the residues of GLU211 and ALA213 in its hinge region. LEU139, GLU211, and ALA213 interacted with hydroxyl group (OH) at C2 position of inhibitors. Mainly, ALA213 interacted with two groups, namely, hydroxyl group (OH) and carboxyl group (C(O)OH) of 5280343, 5280863, and 5280445. The binding mode of the 3H10-5280805 to the receptor was very strong and the bond distance was LEU139 (2.7 Å), GLU260 (1.94 Å), LYS141 (2,14 Å and 2.49 Å), GLU211 (2.38 Å and 1.81 Å), ALA213 (2.17 Å), PRO214 (2.16 Å), and ASH/ASP274 (1.87 Å and 2.14 Å). In 3H10-5280343, bond distance was LEU139 (2.27 Å), ALA213 (2.23 Å and 1.99 Å) and ASH/ASP274 (1.74 Å and 1.72 Å). The 3H10-5280863 is LEU139 (2.21 Å), ALA213 (1.84 Å and 1.63 Å), Å), GLU211 (2.57), ASH/ASP274 (1.87 Å), and 3H10-5280445 was LEU139 (2.21 Å), ALA213 (1.90 Å and 2.02 Å), ASH/ASP274 (1.94 Å), LYS162 (1.87 Å). Therefore, a strong H-bonding network is formed for all the inhibitors. The docking score and hydrogen bond interactions are listed in Table 1. 1. Among these four molecules, 3H10-5280805 has the highest binding affinity with the Glide score and Glide energy (Table 1). Further, 3H10-5280805 had greater number of interactions with the protein.

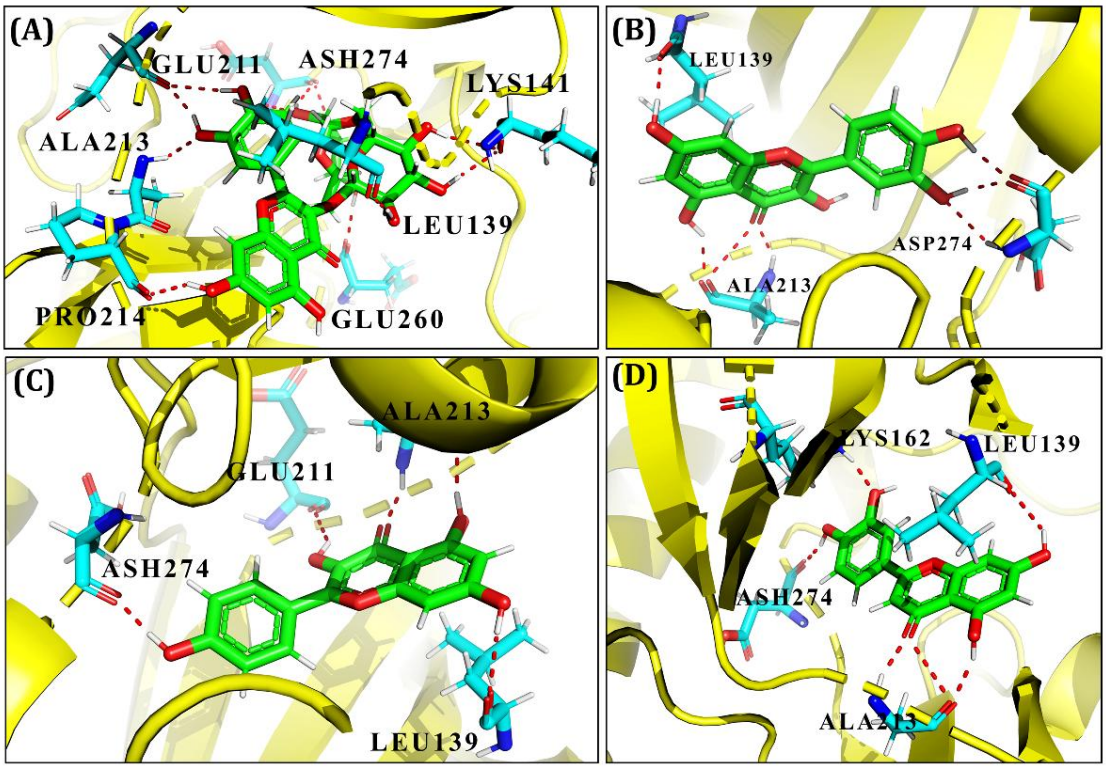

**Figure 2.** The docked protein–ligand complex with hydrogen bond interactions (A. 3H10-5280805, B. 3H10-5280343, C. 3H10-5280863, D, 3H10-5280445).

**Table 1:** Docking studies and their corresponding Glide scores, Glide energy and hydrogen bond interactions.

| S. No | Compound IDs | Glide XP docking | | |
|---|---|---|---|---|
| | | Glide score (kcal mol$^{-1}$) | Glide energy (kcal mol$^{-1}$) | H-bond interactions |
| 1 | 5280805 | -16.66 | -72.227 | LEU139 (2.7 Å), GLU260 (1.94 Å), LYS141 (2,14 Å and 2.49 Å), GLU211 (2.38 Å and 1.81 Å), ALA213 (2.17 Å), PRO214 (2.16 Å), ASH/ASP274 (1.87 Å and 2.14 Å) |
| 2 | 5280343 | -12.54 | -47.789 | LEU139 (2.27 Å), ALA213 (2.23 Å and 1.99 Å), ASH/ASP274 (1.74 Å and 1.72 Å) |
| 3 | 5280863 | -10.64 | -44.308 | LEU139 (2.21 Å), ALA213 (1.84 Å and 1.63 Å), GLU211 (2.57), ASH/ASP274 (1.87 Å) |
| 4 | 5280445 | -10.59 | -35.614 | LEU139 (2.21 Å), ALA213 (1.90 Å and 2.02 Å), ASH/ASP274 (1.94 Å), LYS162 (1.87 Å) |

*2.2. Minimization and density functional theory (DFT) calculations*

*2.2.1. HOMO and LUMO analysis*

The DFT calculations explained the vital properties of the molecular structure [38,39]. These four molecules were carried out by optimizing DFT calculation at the level of B3LYP/6-31G**. The molecules are sparkly in the chemical reactivity, HOMO-LUMO gap increases the charge transfer with the molecule. The molecular orbitals' interactions with the other species together with their energy difference (gap) assists in quantifying the chemical reactivity of the structure which participate in the chemical reactions. Naturally, the electron density is indicated by the intensity of the color that would reflect the characteristic feature of a molecule. Parameters of molecules have been analyzed by chemical reactivity of HOMO, LUMO, and MESP. Commonly, the LUMO serves as an electron acceptor and HOMO serves as an electron donor. The HOMO and LUMO energy gap were analyzed by the stability of the structure. In the HOMO and LUMO, energy gap levels elucidate the fragile nature of reactivity as electron can be transmitted swiftly between the energy levels. In HOMO and LUMO, energy gap of the compounds are 0.15146 eV, (5280805), 0.1449 eV (5280343), 0.14763 eV (5280863), and 0.154 eV (5280445), respectively (Supporting Information, Table Table S3). Thus, the values signify that the molecules are sparkly in the chemical reactivity. The total total energy, dipole moment, HOMO, LUMO, and energy gap affected the stability of the compounds. The HOMO and LUMO plot of the inhibitors are illustrated in Figures 3 and 4. The HOMO-LUMO gap increases the charge transfer with the molecule. The charge transfer and the relation between the HOMO-LUMO gap is attained by the charge transfer with the molecule. These four molecules are plotted in a minimal amount of the HOMO and LUMO energy gap. The

Preprints (www.preprints.org) | NOT PEER-REVIEWED | Posted: 23 August 2019 doi:10.20944/preprints201908.0238.v1



color-coding region was red, indicating the most negative potential region and blue indicating the most positive potential region of the molecules.

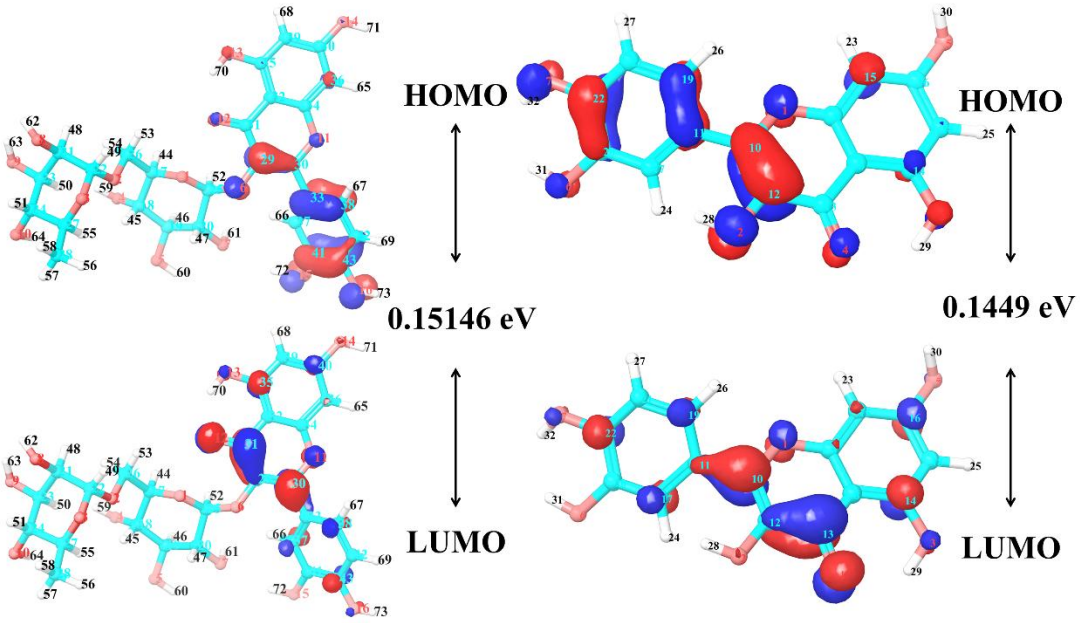


**Figure 3.** Plots of the highest occupied molecular orbital and lowest unoccupied molecular orbital of 5280805 and 5280343.

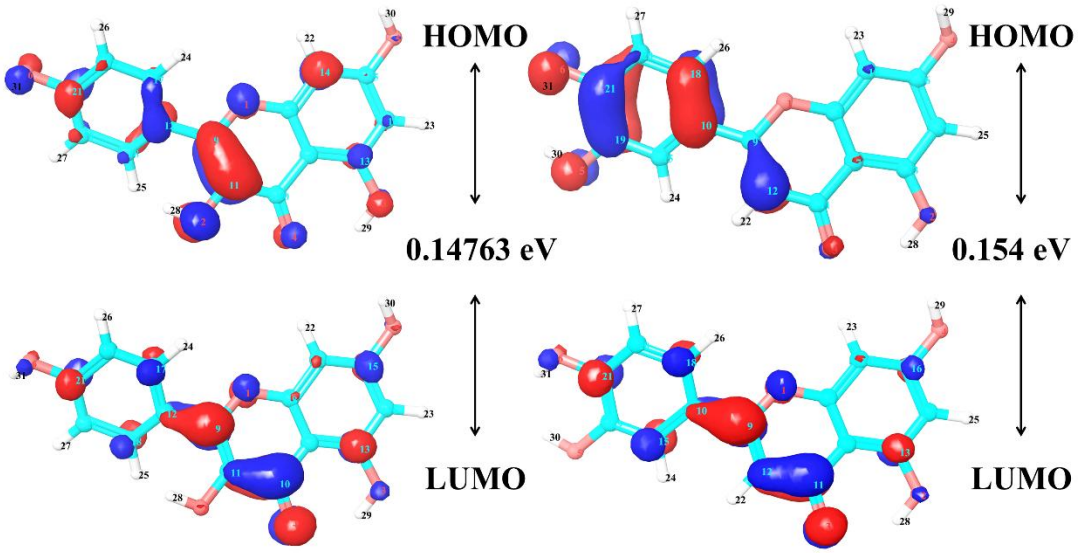


**Figure 4.** Plots of the highest occupied molecular orbital and lowest unoccupied molecular orbital of 5280805 and 5280343.

### 2.2.2. *Molecular electrostatic potential*

The electrostatic potential is a handy descriptor of the knowledge about the sites of electrophilic attack, nucleophilic reactions, as well as hydrogen bonding interactions. The electrostatic potential maps were generated to review the structural aspects of a molecule as it

Preprints (www.preprints.org) | NOT PEER-REVIEWED | Posted: 23 August 2019 doi:10.20944/preprints201908.0238.v1



essentially plays a crucial role in the receptor–ligand interactions. The importance of MESP lines displays the shape, size, negative, positive, as well as neutral electrostatic potential regions of the color grading scheme. It is an important study for likely binding to the receptor site with the shape and size of the molecules. Figure 5 shows the MESP of the molecules. The blue color-coding region (signifying extremely electron deficient region) represents the most positive electrostatic potential and the red coding region (signifying electron rich) represents the most electronegative potential of the molecules. The intermediate color-coding regions are orange, green, and yellow and they prove the charges mid-way between both extremes.

Highly negative ---- red < orange < yellow < green < blue ---- highly positive

The electrostatic map of 5280805 reveals that highly negative points were located at atom O1, atom O3, and atom C23, whereas the highly positive points are located at atom H62, H63, H71, and H73 (Figure 5). The highly electronegative atoms of H63 and H64 interacted with the protein (Aurora kinase A) amino acid residues of ASH/ASP274 and the highly electropositive atoms of H62, H65, and H73 interacted with the residues of LEU139, GLU211, and GLU260 compared to the docking results. Interestingly, the electropositive regions interacted with the active site residues of the protein. The electrostatic map of 5280343 reveals that highly electropositive regions surround atoms H31 and H32 (Figure 5). Furthermore, 5280863 and 5280445, the most electropositive regions surround the atoms H25, H27, H29, H30, and H31 (Figure 5). Majority of the hydrogen represented are in the electropositive region of these four molecules. In all, the compound hydrogen atoms (blue region) react with nucleophilic sites. The electrostatic potential ranges were from −48.228kcal $mol^{-1}$ to 83.30kcal $mol^{-1}$ (5280805), −63.306kcal $mol^{-1}$ to 103.01kcal $mol^{-1}$ (5280343), −62.182 kcal $mol^{-1}$ to 76.694kcal $mol^{-1}$ (5280863), and −48.228 kcal $mol^{-1}$ to 83.307 kcal $mol^{-1}$ (5280445), respectively.

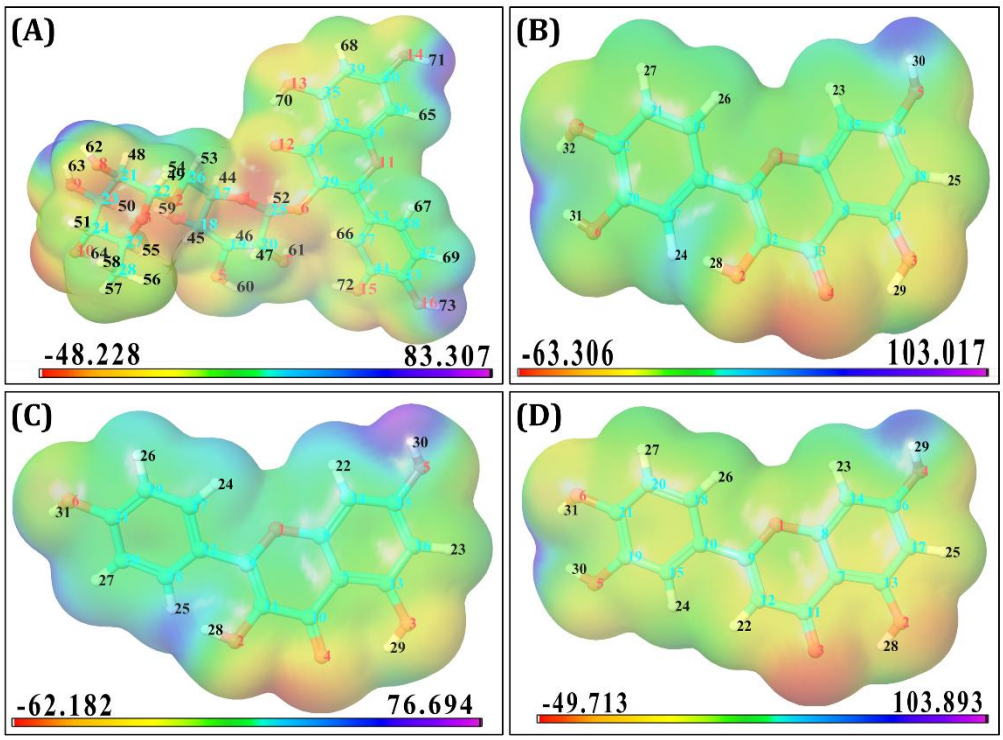

Preprints (www.preprints.org) | NOT PEER-REVIEWED | Posted: 23 August 2019 doi:10.20944/preprints201908.0238.v1



**Figure 5.** Three-dimensional-MESP superimposed on to a surface of constant electron density (.01 e/au3) showing the most positive potential region (deepest blue color) and the most negative potential region (deepest red color) (5280805, 5280343, 5280863 and 5280445).

*2.3. Fukui functions*

Furthermore, the electron density-based local reactivity descriptors of chemical descriptors *viz.*, Fukui functions were projected to deliver deeper insight into the chemical reactivity or selectivity at a specific site of a chemical system [39]. The possibility of nucleophilic and electrophilic attack on atomic sites can be recognized with the aid of Fukui indices. The specific ionization potential, predictor of chemical condensed reactivity, and electron affinity were calculated by the following equation.

$$f^{+} = (\rho^{N+\delta}(r) - \rho^{N}(r))/\delta \text{----------(Nucleophilic attack)}$$

$$f^{-} = (\rho^{N} - \delta(r) - \rho^{N}(r))/\delta \text{----------(Electrophilic attack)}$$

Here, $N$ represents the number of electrons in the reference state of the molecule, and $\delta$ is the fraction of an electron. The Nucleophilic Fukui functions $f^{+}(r)$ and Electrophilic Fukui functions $f^{-}(r)$ for 5280805, 5280343, 5280863, and 5280445 are shown in Figures S1 and S2 (Supporting Information), respectively. The electronegativity for the carbon, nitrogen, and oxygen atoms were greater than the hydrogen atoms prone to nucleophilic attack, making the hydrogen atoms electron deficient regions.

*2.4. Quantum polarized ligand docking*

The improved docking accuracy of QPLD predicted the accurate binding mode between Aurora kinase A and identified four molecules. It is known that the accuracy of electric charges plays a crucial role in ligand-protein interactions. The quantum mechanical calculations were obtained from the inhibitor changes in the binding site region of the protein. The redocking of these four compounds with QM/MM charges could lead to an enhanced docking precision of the ligand-protein complexes. Results of QPLD were associated with the Glide XP docking results (Supporting Information, Table S4) and it was shown that all the compounds had good fit in the active site of Aurora kinase A protein. Among these four molecules, 5280805 has high binding affinity and more stability in the active site of AURKA.

*2.5. Binding free energy calculation*

The Prime MM-GBSA method was calculated by the free energy ($\Delta G_{bind}$) of the selected inhibitors against Aurora kinase A. In Glide docking, XP docking poesis and QPLD poesis were obtained to perform MM-GBSA calculation and this was done using surface area energy, salvation energy, and energy minimization of the protein ligand complexes. The results of the energetic analysis of the complexes are provided in Supporting Information Table S5. Prime MM/GBSA ($DG_{Bind}$) range was from −97.82 kcal $mol^{-1}$ (5280805), −70.51 kcal $mol^{-1}$ (5280343), −65.51 kcal $mol^{-1}$ (5280863), and −63.74 kcal $mol^{-1}$ (5280445). Among these four molecules, 5280805 have a high binding

binding score compared to 5280343, 5280863, and 5280445. The results show that, more promising contributions to the ligand binding were non-polar salvation terms ($\Delta G_{lipo}$), van der Waals ($\Delta G_{vdW}$), and covalent energy ($\Delta G_{covalent}$). These identified inhibitors do not represent any important changes in their binding free energies.

*2.6. Molecular dynamics simulation*

The protein ligand complexes were performed by MD simulation study to examine the stability of the compounds to the binding site of Aurora kinase A protein. MD simulation deals with studying the behavior of protein and ligand for a particular time. The dynamic properties of the protein were evaluated based on the topology of native contacts in biological functions [40]. The crystal structure of the protein is more helpful for comparing the global motions and is observed in the experimental changes. The computational methods could be advantageously engaged for evaluating protein flexibility. The whole simulation was subjected for 100 ns in the production phase for the ligand complexes. In addition, the number of default parameters used stabilized the system.

*2.6.1 Root mean square displacement*

The structure and dynamic proprieties of the protein ligand complexes were analyzed as the backbone RMSDs during the simulation period of 100 ns. The RMSD was measured as the average distance between the backbone atoms of the protein-ligand structures and it was derived from the following equation.

$$\mathrm{RMSD} = \sqrt{\frac{1}{N}\sum_{i=0}^{N}\delta_i^2}$$

where $N$ represents the total number of atoms considered in the calculation and δ represents the distance between the $N$ pairs of equivalent atoms. The backbone RMSD of the Aurora kinase A is presented in Figure 6. The RMSD of 3H10-5280863 was observed at a very small deviation at 04.5 nm from 0 to 30 ns and it was stabilized after 30 ns. Among these four RMSDs, the RMSD of 3H10-5280805 was more stable during stabilization throughout simulation compared to 3H10-5280343 and 3H10-5280863 (Figure 6). The RMSD of the ligands are illustrated in Figure 7. In the ligand, RMSD of 3H10-5280343 fluctuated more from the beginning to 100 ns. For the RMSD of 3H10-5280805 and 3H10-5280863, a more stable time of 100 ns was observed (Figure 7). In 3H10-5280445, there was a small fluctuation at 01.5 nm during the simulation period of 100 ns. Moreover, the hydrogen bond interacting with the active site residues were LEU139, GLU211, and ALA213 of the 3H10. The hydrogen bond interactions throughout the simulation period of 100 ns are displayed in Figure 8.

Preprints (www.preprints.org) | NOT PEER-REVIEWED | Posted: 23 August 2019 doi:10.20944/preprints201908.0238.v1



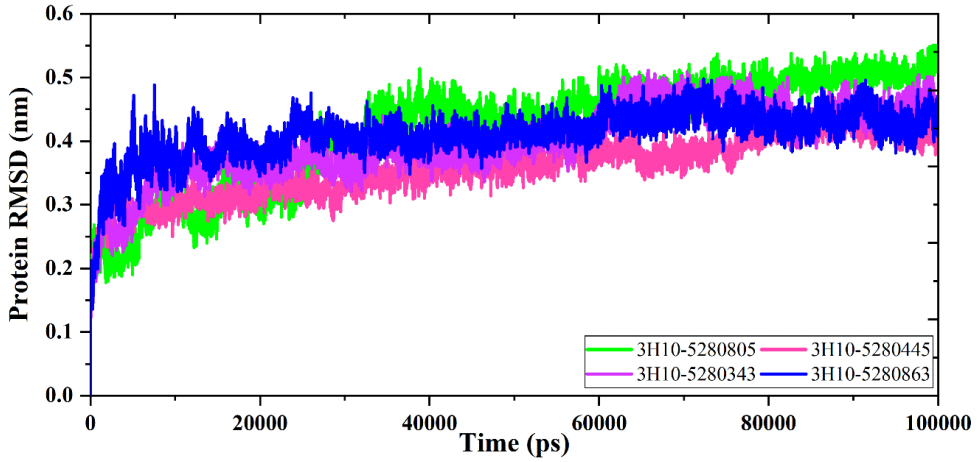


314

315 **Figure 6.** The RMSD of the backbone atom of the 3H10 (Aurora kinase A) over a time period of 100
316 ns.

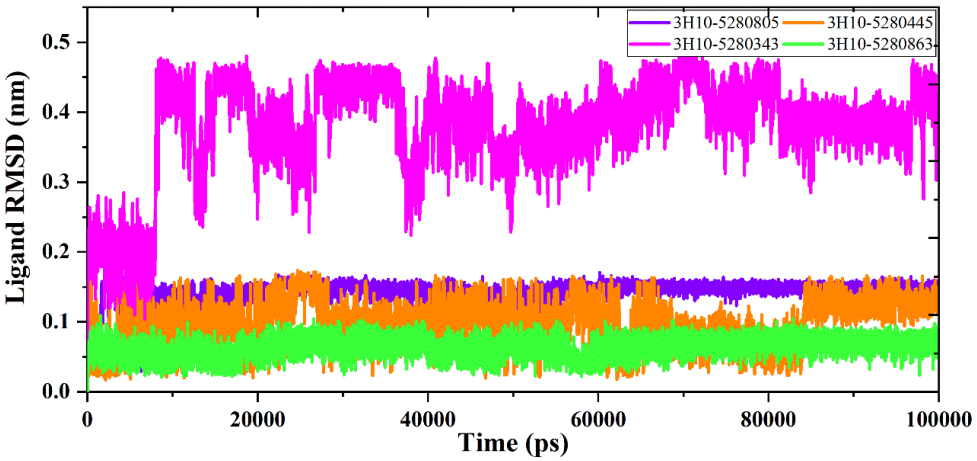


317

318 **Figure 7**. The RMSD of 5280805, 5280343, 5280863 and 5280445 in the active site of 3H10 (Aurora
319 kinase A).

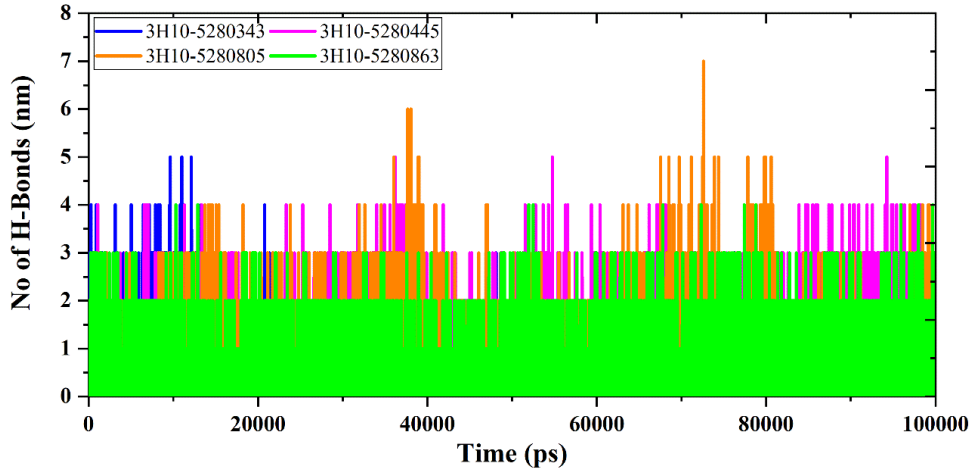


320

321 **Figure 8.** The total number of the hydrogen bonds produced during the simulation period of 100 ns.

 doi:10.20944/preprints201908.0238.v1



*2.6.2. Root mean square fluctuation*

The root mean square fluctuations (RMSF) were assessed and plotted to equate the flexibility of each residue in the–ligand-protein complexes. The RMSF of the protein ligand complex denoted the minimized fluctuation for all the complexes (Supporting Information, Figure S3). The RMSF did not deviate much during the simulation period of 100 ns and the average RMSF values were kept constant for all the complexes.

Furthermore, we have analyzed that the stabilized systems are plotted by potential energy, total energy, pressure energy, and temperature energy. These parameters analyzed by the system were stable during the MD simulation (Supporting Information, Figure S4–S7). The average potential energy value is found at −908132.7723kcal/mol$^{-1}$ (3H10-5280343), −907975.0827 kcal/mol$^{-1}$ (3H10-5280445), −907739.6851kcal/mol$^{-1}$ (3H10-5280805), and −908150.0474kcal/mol$^{-1}$ (3H10-5280863). Thus, the overall standard deviation for potential energy are −908132.7723kcal/mol$^{-1}$ (3H10-5280343), −907975.0827kcal/mol$^{-1}$ (3H10-5280445), −907739.6851kcal/mol$^{-1}$ (3H10-5280805), and −1062.344992kcal/mol$^{-1}$ (3H10-5280863). The average total energy (kcal/mol$^{-1}$) values are −739738.1729 (3H10-5280343), −739602.9632 (3H10-5280445), −739283.4609 (3H10-5280805), and −739756.31 (3H10-5280863), whose standard deviation for total energy was 1357.733885, 1366.734671, 1382.685931, and 1359.663651, respectively. The results denoted that the potential energy and total energy reached equilibrium at the particular temperature of 300 K.

*2.6.3. Radius of gyration*

The structural flexibility of the complexes was analyzed by plotting the radius of gyration (Rg). The calculated Rg values of the 3H10 with four molecules are shown in Figure S8 (Supporting Information). The Rg value represents the mass weighted root mean square distance of an atom collection from their common center of mass. The parameters of these complexes are more stable during the simulation of 100 ns. The Rg plots of 3H10 with 5280343, 5280445, and 5280805 have similar patterns with the average Rg values in the region at 1.9 nm (Supporting Information, Figure S8). Moreover, the 3H10-5280863 deviates slightly from 1.95 to 2.0 nm. All the four compounds and 3H10 are formed by constant Rg values throughout the simulation period of 100 ns (Supporting Information, Figure S8).

*2.7. Mass action kinetics*

The literature survey was carried out with the aim of identifying and gleaning the necessary necessary information for cancer. Apart from that, pharmacokinetics pathway was also created to ascertain the efficacy of the drug. While the nodes in the pathway signify the entities, the edges denote the node connectivity. Pharmacokinetics was carried out with concentrated doses of 0.40 µm. µm. Potential of the drug was established with an in-silico biochemical pathway of cancer, which in sequence was premeditated with a biology workbench of computational systems. Also employed in indicating the adequacy as well as suitability of the testing drug is the kinetics simulation or pharmacokinetics simulation. At therapeutic doses, most drugs' pharmacokinetics is of first-order

Preprints (www.preprints.org) | NOT PEER-REVIEWED | Posted: 23 August 2019 doi:10.20944/preprints201908.0238.v1



reaction, and the Michaelis–Menten equation or mass kinetics equation can be handy to determine the non-linear kinetics scheme. To investigate the relationship, mechanism and interaction between biological organizations, it is pertinent to use biological network representations. Evidence from the literature has also shown that pharmacokinetic mechanism of cancer has been investigated with biochemical mathematical theories and models. Figures 9 illustrate pharmacokinetics simulation; similar results were also obtained with an experimentally reported concentration. The interactions and mechanism among entities can be explained with representations of biological networks. The pharmacokinetic mode of cancer can be investigated using biochemical models (Figure 10). Report from experimental studies also shows the hostile effects of cancer. What's more, similar results have been obtained with the concentration reported in other experiments. The down regulation of entities entities is manifested in the graph (Figure 10), and this trend represents the inhibition of cancer.

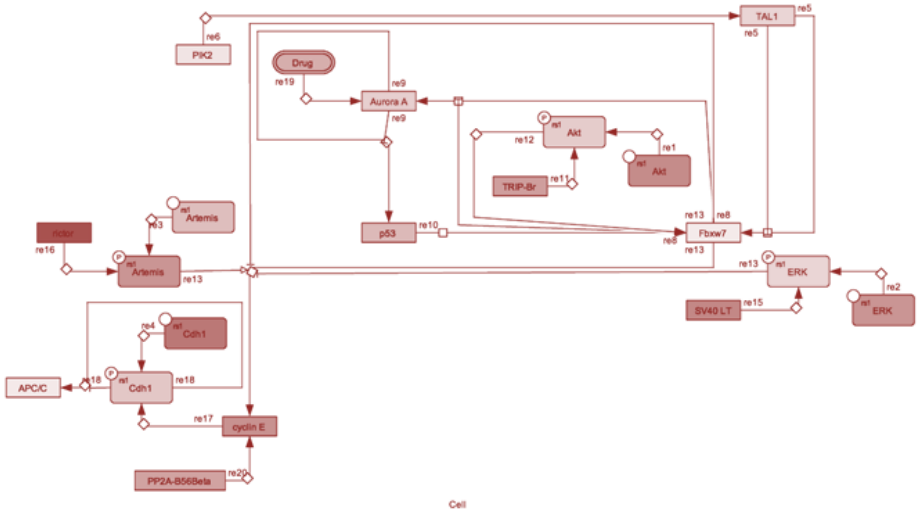


**Figure 9.** Representation of biochemical pathway of cancer in presence of Compound 1 to 4.

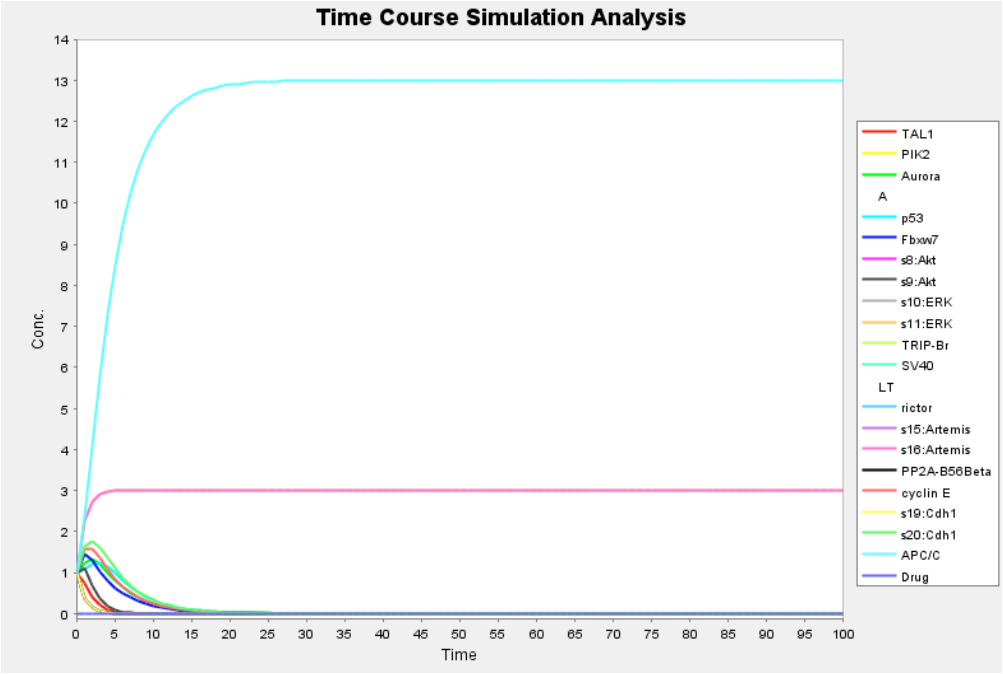

**Figure 10.** Representation of Time course simulation of entire pathway in presence of Compound1.

## 3. Discussion

The Aurora family (Aurora A, Aurora B, and Aurora C) belongs to the serine/threonine protein kinases [41]. The Aurora kinase family has emerged as an important target family for cancer therapies. The Aurora kinases play a crucial role in cell division and primarily active during mitosis. mitosis. Although, the three Aurora kinases are expressed in all dividing cells, whereas Aurora kinase A is found at the centrosome in the mitotic cells from late S and G2 phases until telophase, but but is also localized to the spindle throughout mitosis [41]. Aurora kinase A are highly homologous in sequence, particularly ATP-binding sites. The molecular constraints of the ATP binding site are an an essential step for designing inhibitors. Fancelli *et al.,* (2005) [42] identified the ATP-binding pocket pocket of the Aurora kinase A, which can be divided into five areas (kinase hinge region, solvent accessible region, sugar region, phosphate-binding region and buried region). Hence, the hinge region (residues 210-216) plays a vital role in forming the catalytic active site. From the results of the the *in silico* analysis it has been established that, the selected four inhibitors had H-bonding interactions with the active site of Aurora kinase A, especially GLU211and ALA213. Further these inhibitors had better binding affinity towards the active site of AURKA. Finally, system biology experiments were validated. We mapped a broad range of disorders onto the network, before focusing more specifically on cancer. Disease pathway "modules" or clusters are known to form within molecular networks, showing overlap with functional modules. Cancer genes have been found to be especially highly connected with different types of cancer, forming highly connected overlapping modules. Our representation provides a higher-level view of the pathways and functions affected by diseases, without the inaccuracies inherent in molecular-level interaction data. It has been suggested in previous studies that, quercetin (5280343) promotes effects of Ni on human lung cancer cell invasion and migration. Further, it was reported that quercetin has ability to regulate and control the lung cancer targeting through a number of pathways namely Snail-dependent Akt activation, Snail-independent disinterring and metalloproteinase domain-containing protein9 (ADAM9) expression pathways [43,44]. And also toll-like receptor 4 (TLR4) / nuclear factor kappa-light-chain-enhancer of activated B cells (NF-κB) signaling [45], c-Jun N-terminal kinases (JNK) and mitogen-activated protein kinases (MAPK) pathways [46] in lung cancer cells and animal models. Notably, Xingyu *et al.,* (2016) [47] reported that quercetin suppresses suppresses lung cancer growth by targeting Aurora B kinase in JB6 Cl41 and A549 lung cancer cells. Kaempferol (5280863) inhibits proliferation, invasion and migration of cancer cell through down-regulation of AKT and focal adhesion kinase (FAK) Pathways [48]. Also, kaempferol induced apoptosis and autophagy through up-regulating miR-340 [49], along with up-regulation of PTEN and inactivation of the PI3K/AKT pathway [50,51,52]. Kaempferol is a tetrahydroxy flavone in which which the four hydroxy groups are located at positions 3, 5, 7 and 4'. Acting as an antioxidant by reducing oxidative stress, it is currently under consideration as a possible cancer treatment. Moreover, studies reported that Luteolin (5280445) suppress the tumor growth through the activation of nuclear factor (NF)-κB signaling, regulation of microRNA-34a-5p [53], downregulation of TAM receptor tyrosine kinases [54], phosphoinositide-dependent kinase-1 (PDK1), Akt [55] and signal transducer and activator of transcription 3 [56] signaling pathways. Zhou *et al.,* (2017) reported that luteolin induces G0/G1 arrest and pro-death autophagy through the reactive oxygen

 doi:10.20944/preprints201908.0238.v1



species-mediated AKT/mTOR/p70S6K signaling pathway [57]. Luteolin is an important dietary component of food and plant-based beverages, which have been reported to exhibit health beneficial properties, such as anti-apoptosis, anti-oxidative, antihyperuricemia, antiinflammation, and anti-hyperlipidemia [58]. The rutin inhibits the cancer cell growth by cell cycle arrest and/or apoptosis, along with inhibition of proliferation, angiogenesis, and/or metastasis in colorectal cell lines [59]. Consequently, rutin (5280805) has demonstrated that it inhibits the proliferation, attenuates superoxide production, decreases adhesion and migration of human cancerous cells through tumor necrosis factor alpha expression [60], NF-κB signaling [61] and regulation of glycogen synthase kinase (GSK-3β) [62]. These experimental reports support the present study and indicates that quercetin, kaempferol, luteolin and rutin could be potent inhibitors of AURKA. Based on this information and in *silico* analysis, these four inhibitors could be potent inhibitors against AURKA.

## 4. Materials and methods

### *4.1. Ligand synthesis*

The compounds were used in our perverse study [18-34] and these compounds were identified from mangrove species using GC-MS analysis. These identified three-dimensional structure of the molecules [18-22] were downloaded from the PubChem database, and these structures were assigned by LigPrip (LigPrep, Schrödinger, LLC, New York, NY, 2018-3 ). The structures were changed into MAE (Maestro) format and standardized by OPLS 2005 force field with default settings.

### *4.2. Preparation of structure*

The X-ray crystallographic structures of Aurora kinase A was obtained from the protein databank (http://www.rcsb.org/), with accession ID 3H10. This AURKA was carried out by protein preparation wizard of the Glide software (Schrödinger Suite 2018-3 Protein Preparation Wizard) and it was minimized with the help of OPLS-2005 force field. Weaker restraints were applied to the non-hydrogen atoms and refinement was carried out as per the recommendations of Schrödinger Suite 2018-3 Protein Preparation Wizard. The OPLS-2005 force field is more sensitive at an intermediate docking stage and provides finer geometric details than other docking tools. The most probable positions of hydroxyl, protonation states, thiol hydrogen atoms, and Chi 'flip' assignments for Asn, Gln, and His residues and tautomers of His residues were chosen by the protein assignment script of Schrödinger. The minimizations were done till the average root mean square deviation of the non-hydrogen atoms attained 0.3 Å.

### *4.3. Active site predictions and molecular docking*

SitMap was used to find the binding site of the AURKA in Maestro (SiteMap, Schrödinger, LLC, New York, NY, 2018-3) with default parameters. Maps were created to divulge the binding cavity of the protein. Likely binding sites were recognized with several physical descriptors such as

hydrophobic, hydrogen bonding, linking site points, hydrophilic, a degree of exposure, size, a degree of enclosure, and tightness.

The molecular docking was used to examine the binding interaction between the protein–ligand complexes [33-36]. The LCMS identified molecules were carried out by docking study in the binding site of 3H10 human protein using Glide SP and XP module (Glide, Schrödinger, LLC, New York, NY, 2018-3). The properties and shape of the receptors were characterized on a grid by several arrays of fields that provide more precise scoring to the molecules. The grid was generated with 90x80x60 grid points in XYZ and grid spacing of 0.375 Å. The hydrogen bonding constraints and geometry were applied for substrate docking study. Default parameters were performed by the experiments. Extraprecision (XP) algorithm was used in the active site of Aurora A protein. The top-ranking poses were chosen based on the Glide score for further analysis. Lastly, the top four compounds were taken for further studies.

### *4.4. Minimization and Density Functional Theory Calculations*

The selected four molecules were minimized by MacroModel (MacroModel, Schrödinger, LLC, New York, NY, 2018-3) by a OPLS_2005 force field with solvation, water, and convergence conditions. Conformational search was performed by mixed MCMM/low-mode search with 1000 steps per rotatable bond, and 21kJ/mol$^{-1}$ energy window was utilized for retention conformers. Recognized conformers were performed by DFT using Jaguar (Schrödinger Release 2018-3: Jaguar, Schrödinger, LLC, New York, NY, 2018). DFT calculations were done to know the electronic molecular features *viz.*, electron density, molecular electrostatic map, and frontier molecular orbital density fields, which can elucidate the biological activity and molecular features (eg. the lowest unoccupied molecular orbital and highest occupied molecular orbital). These compounds were calculated by DFT using Schrödinger Release 2018-3: Jaguar, Schrödinger, LLC, New York, NY, 2018 depending on the solvation state. The conformers were analyzed via Lee–Yang–Parr correlation functional (B3LYP) and Becke's three-parameter exchange potential4 [63-65 ] using 6-31G** basic set level [66,67]. The implicit salvation model of Poisson Boltzmann Finite (PBF) was employed with single point calculations. In the present study, 3D molecular electrostatic potentials (MESP) $V(r)$ at a point $r$ owing to a molecular system with nuclear charges $\{ZA\}$ situated at $\{R_A\}$ and an electron density $\rho(r)$ were obtained by the following equation:

$$V(r) = \sum_{A=1}^{N} \frac{Z_A}{|r - R_A|} - \int \frac{\rho(r')d^3r'}{|r - r'|}$$

In the above equation, $N$ denotes the total nuclei count in the molecules and the two terms indicate the bare nuclear potential and the electronic contributions, respectively. The molecular electrostatic properties were computed with a dipole moment, HOMO, LUMO energy, and MESP. The electrostatic potentials were assessed using van der Waals (vdW) contact surface area of the molecule. The Color-coded surface values indicate the positive electrostatic potentials and the overall molecular size. The deepest blue color indicates the most positive electrostatic potential regions and the deepest red color indicates the most negative electrostatic potential regions. The medium yellow, green shades, and orange represent intermediate ranges of reactivity. Further, the Fukui functions were calculated; they represent the changes in the molecular electron density while

Preprints (www.preprints.org) | NOT PEER-REVIEWED | Posted: 23 August 2019 doi:10.20944/preprints201908.0238.v1



adding or removing charges. Jaguar calculates Fukui functions in a finite-difference strategy as follows:

$$f^{+} = (\rho^{N+\delta}(r) - \rho^{N}(r))/\delta$$

$$f^{-} = (\rho^{N-\delta}(r) - \rho^{N}(r))/\delta$$

where $N$ denotes the number of electrons in the reference state of the molecule, and $\delta$ is the fraction of an electron.

*4.5. Quantum Polarized Ligand Docking*

The four compounds were subjected to an enhanced docking method of QPLD analysis (Schrödinger Suite 2018-3 QM-Polarized Ligand Docking protocol; Glide, Schrödinger, LLC, New York, NY). The QPLD has integrated quantum mechanical and molecular mechanical (QM/MM) calculations [68,69]. Three steps of docking were performed by QPLD; the normal Glide docking with the best ligand served as the first step. In the second step, the partial charges in the ligand atoms were replaced with the field of the receptor for the ligand complex, and the changes were assessed using the QM calculations. B3LYP density functional theory and 6-31G**/LACVP* base set was used with single point electrostatic calculation. The "Ultrafine" SCF accuracy level (iacc = 1, iac-scf = 2) was employed for the QM region. In the final step, the ligand was redocked with the updated atomic charges using Glide XP and QPLD [70].

*4.6. Prime/MM-GBSA Calculations*

The docking complexes were carried out using MM-GBSA calculation (Schrödinger Release 2018-3: Prime, Schrödinger, LLC, New York, NY, 2018). The docked complexes were minimized by using local optimization feature in Prime. The OPLS-AA 2005 force field was employed for determining the binding energy for a set of receptor and ligand. The following equation was used for calculating the binding free energy:

$$\Delta G_{Bind} = \Delta E_{MM} + \Delta G_{Solv} + \Delta G_{SA}$$

Here, $\Delta E_{MM}$ is the variance between the minimized energy of the protein-ligand complexes, while $\Delta G_{Solv}$ is the variation between the GBSA solvation energy of the protein-ligand complexes and the sum of the solvation energies for the protein and ligand. In $\Delta G_{SA}$ contains some of the surface area energies in the protein and ligand and the difference in the surface area energies for the complexes. The minimization of the docked complexes was performed using a local optimization feature of Prime.

*4.7. Molecular Dynamics Simulation*

The docking complexes were carried out by molecular dynamics (MD) simulation studies using Gromacs along with GROMOS96 43a force field [71-73]. The GROMACS topology of the molecules was generated by the PRODRG server [74] and Automatic Topology Builder server [75-77]. The system was solvated with SPC (simple point charge) water model. Proper counter ions and the cubic cell were supplemented to fulfill the electro neutrality of the system. Minimization of

 doi:10.20944/preprints201908.0238.v1



all the atoms using the steepest descent minimization algorithm for 50,000 steps and tolerance of 100 kJ/mol$^{-1}$ [78] was subsequent to neutralization process. The system was equilibrated with NVT (same number of particles, volume, and temperature) ensemble and NPT (same number of particles, pressure, and temperature) ensemble. V-rescale was employed to monitor temperature (weak coupling method). The covalent interactions were constrained with the help of LINCS (Linear Constraint Solver) algorithm. The system was equilibrated with pressure, temperature, etc., and the equilibrated system was applied in generating MD run of 100 ns with a time step of 2 fs at 300k. Long-range electrostatic interactions were determined by Particle Mesh Ewald (PME) algorithm [79]. The atomic structural coordinates were stored with an interval of 2 ps. The trajectories acquired from each run were investigated using various modules of Gromacs; g_rmsd, g_rmsf, g_energy, g_sas, etc.

### *4.8. Mass action kinetics*

Mass action kinetics are used in chemical engineering and chemistry fields to demonstrate the direct relationship between the rate of reaction and the product of the concentration of reactants; with mass action kinetics, researchers can accurately predict whether a chemical reaction is second-order, first-order, zero-order, or reversible reactions.

The simple differential equation of mass-action kinetics generates polynomial vector fields. For instance,

$$A + B \rightarrow C$$

$$[\text{rate of chemical reaction}] \ \alpha \ [A][B] \text{ or } [\text{rate of reaction}] = k[A][B]$$

where [B] and [A] represent the concentrations of *B* and *A*, respectively, and k denotes the rate constant or proportionality rate. This value is always greater than zero, and it is influenced by the temperature of the reactants. Hence, the rate of chemical reaction can be written as follows:

$$\frac{d[A]}{dt} = -k[A][B]$$

$$\frac{d[B]}{dt} = -k[A][B]$$

$$\frac{d[C]}{dt} = k[A][B]$$

## 5. Conclusion

In summary, this study identified inhibitors against AURKA and identified four inhibitors using various *in silico* analysis. The computational studies provided deeper structural insight to the interacting residues of LEU139, GLU211, and ALA213 with the hinge region of AURKA.

Furthermore, the molecular dynamics simulation was used to understand the conformational changes on the ligand protein complexes. In MM-GBSA analysis, the molecular docking studies were validated and it was shown that the derivative molecules were a binding capably of the AURKA. Also, density functional theory calculations were confirmed for a small amount of HOMO–LUMO energy gap. These computational studies indicated that, the binding properties of the inhibitors could be utilized as potential therapeutic agents against Aurora kinase A.

**Author Contributions:** S.C., G.S., and D.-Q.W. conceived and designed the experiment S.C., G.S., S.K., and D.-Q.W. wrote the main manuscript text. C.S., and S.K.S., performed the molecular docking studies. A.C.K., performed the experimental validation. S.K., K.G., and A.S.N., formatted the manuscript and figures according to the instructions. S.C., G.S., and D.-Q.W., critically reviewed the manuscript. All the authors approved the final manuscript.

**Acknowledgments**

The authors duly acknowledge the financial support of the Ministry of Science and Technology of China (Grant No.: 2016YFA0501703), Henan Natural Science (Grant No.: 162300410060), grants from the State Key Lab on Microbial Metabolism, and joint research funds for Medical and Engineering and Scientific Research at Shanghai Jiao Tong University (YG2017ZD14) to DQ.W.; Henan Postdoctoral Science Foundation (Grant No.: 001802029 and 001803035) to S.K. and G.S; and China Postdoctoral Science Foundation (Grant No.: 2018M632766) to G.S.; The simulations in this work were supported by the Center for High Performance Computing, Shanghai Jiao Tong University, China.

**Conflict of interest**

All authors declared that they do not have any conflict of interest to publish this manuscript in Marine Drugs.

**References**

1. Tang, A.; Gao, K.; Chu, L.; Zhang, R.; Yang, J.; Zheng, J. Aurora kinases: novel therapy targets in cancers. *Oncotarget.*, 2017, *8* (14), 23937-23954. [CrossRef] [PubMed]
2. Goldenson, B.; Crispino, J.D. The aurora kinases in cell cycle and leukemia. *Oncogene*. 2015, 29;34(5):537-45. [CrossRef] [PubMed]
3. Lampson, M.A.; Cheeseman, I.M. Sensing centromere tension: Aurora B and the regulation of kinetochore function. Trends *Cell Biol.* 2011, 21(3):133-40. [CrossRef] [PubMed]
4. Jacobsen, A.; Bosch, L.J.W.; Martens-de Kemp, S.R; Carvalho, B.; Sillars-Hardebol, A.H.; Dobson, R.J.; de Rinaldis, E.; Meijer, G.A.; Abeln, S.; Heringa, J.; Fijneman, R.J.A.; Feenstra, K.A. Aurora kinase A (AURKA) interaction with Wnt and Ras-MAPK signalling pathways in colorectal cancer. *Sci Rep.* 2018, 14;8(1):7522. [CrossRef] [PubMed]
5. Zhong, N.; Shi, S.; Wang, H.; Wu, G.; Wang, Y.; Ma, Q.; Wang, H.; Liu, Y.; Wang, J. Silencing Aurora-A with siRNA inhibits cell proliferation in human lung adenocarcinoma cells. *Int J Oncol.* 2016, ;49(3):1028-38. [CrossRef] [PubMed]
6. DuBois, SG.; Marachelian, A.; Fox, E.; Kudgus, R.A.; Reid, J.M.; Groshen, S.; Malvar, J.; Bagatell, R.; Wagner, L.; Maris, J.M.; Hawkins, R.; Courtier, J.; Lai, H.; Goodarzian, F.;

Shimada, H.; Czarnecki, S.; Tsao-Wei, D.; Matthay, K.K.; Mosse, Y.P. Phase I Study of the Aurora A Kinase Inhibitor Alisertib in Combination With Irinotecan and Temozolomide for Patients With Relapsed or Refractory Neuroblastoma: A NANT (New Approaches to Neuroblastoma Therapy) Trial. *J Clin Oncol.* 2016, 20;34(12):1368-75. [CrossRef] [PubMed]

7. Shaikh, M.H.; Idris, A.; Johnson, N.W.; Fallaha, S.; Clarke, D.T.W.; Martin, D.; Morgan, I.M.; Gabrielli, B.; McMillan, N.A.J. Aurora kinases are a novel therapeutic target for HPV-positive head and neck cancers. *Oral Oncol.* 2018, 86:105-112. [CrossRef] [PubMed]
8. Ding, L.; Yang, L.; He, Y.; Zhu, B.; Ren, F.; Fan, X.; Wang, Y.; Li, M.; Li, J.; Kuang, Y.; Liu, S.; Zhai, W.; Ma, D.; Ju, Y.; Liu, Q.; Jia, B.; Sheng, J.; Chang, Z. CREPT/RPRD1B associates with Aurora B to regulate Cyclin B1 expression for accelerating the G2/M transition in gastric cancer. *Cell Death Dis.* 2018, 5;9(12):1172. [CrossRef] [PubMed]
9. Zhang, Y.; Jiang, C.; Li, H.; Lv, F.; Li, X.; Qian, X.; Fu, L.; Xu, B.; Guo, X. Elevated Aurora B expression contributes to chemoresistance and poor prognosis in breast cancer. *Int J Clin Exp Pathol.* 2015,1;8(1):751-7. [CrossRef] [PubMed]
10. Zhao, H.; Owen, S.; Davies, E.L.; Jiang, W.G.; Martin, T.A. The Effect of Aurora Kinase Inhibitor on Adhesion and Migration in Human Breast Cancer Cells and Clinical Implications. *World J Oncol.* 2017, 8(5):151-161. [CrossRef] [PubMed]
11. Selvaraj, G.; Kaliamurthi, S.; Kaushik, A.C.; Khan, A.; Wei, Y.K.; Cho, W.C.; Gu, K.; Wei, D.Q. Identification of target gene and prognostic evaluation for lung adenocarcinoma using gene expression meta-analysis, network analysis and neural network algorithms. *J Biomed Inform.* 2018, 86:120-134. [CrossRef] [PubMed]
12. Hole, S.; Pedersen, A.M.; Lykkesfeldt, A.E.; Yde, C.W. Aurora kinase A and B as new treatment targets in aromatase inhibitor-resistant breast cancer cells. *Breast Cancer Res Treat.* 2015,149(3):715-26. [CrossRef] [PubMed]
13. Kantarjian, H.M.; Schuster, M.W.; Jain, N.; Advani, A.; Jabbour, E.; Gamelin, E.; Rasmussen, E.; Juan, G.; Anderson, A.; Chow, V.F.; Friberg, G.; Vogl, F.D.; Sekeres, M.A. A phase 1 study of AMG 900, an orally administered pan-aurora kinase inhibitor, in adult patients with acute myeloid leukemia. *Am J Hematol.* 2017, 92(7):660-667. [CrossRef] [PubMed]
14. Diamond, J.R.; Eckhardt, S.G, Pitts, T.M.; van Bokhoven, A.; Aisner, D.; Gustafson, D.L.; Capasso, A.; Sams, S.; Kabos, P.; Zolman, K.; Colvin, T.; Elias, A.D.; Storniolo, A.M.; Schneider, B.P.; Gao, D.; Tentler, J.J.; Borges, V.F.; Miller, K.D. A phase II clinical trial of the Aurora and angiogenic kinase inhibitor ENMD-2076 for previously treated, advanced, or metastatic triple-negative breast cancer. *Breast Cancer Res.* 2018, 2;20(1):82. [CrossRef] [PubMed]
15. Niu, H.; Shin, H.; Gao, F.; Zhang, J.; Bahamon, B.; Danaee, H.; Melichar, B.; Schilder, R.J.; Coleman, R.L.; Falchook, G.; Adenis, A.; Behbakht, K.; DeMichele, A.; Dees, E.C.; Perez, K.; Matulonis, U.; Sawrycki, P.; Huebner, D.; Ecsedy, J. Aurora A Functional Single Nucleotide Polymorphism (SNP) Correlates With Clinical Outcome in Patients With Advanced Solid Tumors Treated With Alisertib, an Investigational Aurora A Kinase Inhibitor. *EBioMedicine.* 2017, 25:50-57. [CrossRef] [PubMed]
16. Schöffski, P.; Besse, B.; Gauler, T.; de Jonge, M.J.; Scambia, G.; Santoro, A.; Davite, C.; Jannuzzo, M.G.; Petroccione, A.; Delord, J.P. Efficacy and safety of biweekly i.v. administrations of the Aurora kinase inhibitor danusertib hydrochloride in independent

cohorts of patients with advanced or metastatic breast, ovarian, colorectal, pancreatic, small-cell and non-small-cell lung cancer: a multi-tumour, multi-institutional phase II study. *Ann Oncol.* 2015, 26(3):598-607. [CrossRef] [PubMed]

17. Falchook, G.S.; Bastida, C.C.; Kurzrock, R. Aurora Kinase Inhibitors in Oncology Clinical Trials: Current State of the Progress. *Semin Oncol.* 2015, 42(6):832-48. [CrossRef] [PubMed]
18. Selvaraj, G.; Kaliamurthi, S.; Thirugnanasambandam, R., Influence of Rhizophora apiculata Blume extracts on $\alpha$-glucosidase: Enzyme kinetics and molecular docking studies. *Biocatal Agric Biotechnol.* 2015, 4(4):653-660.
19. Selvaraj, G.; Kaliamurthi, S.; Thirugnasambandan R., Effect of dichloromethane fraction of Rhizophora mucronata on carbohydrate, lipid and protein metabolism in type 2 diabetic rats. *Integr Obesity diabetes* 2017, 3:1-8.
20. Satyavani, K.; Gurudeeban, S.; Manigandan, V.; Rajamanickam, E.; Ramanathan, T., Chemical compositions of medicinal mangrove species Acanthus ilicifolius, Excoecaria agallocha, Rhizophora apiculata and Rhizophora mucronata. *Curr Res Chem* 2015, 7 (1), 1-8.
21. Selvaraj, G.; Kaliamurthi, S.; Thirungnasambandam, R.; Vivekanandan, L.; Balasubramanian, T., Anti-nociceptive effect in mice of thillai flavonoid rutin. *Biomed Environ Sci* 2014, 27 (4), 295-299.
22. Satyavani, K.; Gurudeeban, S.; Ramanathan, T.; Muthusankar, A., Influence of Rhizophora apiculata flavonoids on chemical and thermal induced nociceptive models. *Methodology* 2012.
23. Selvaraj, G.; Kaliamurthi, S.; Ekambaram, R.; Thirugnanasambandan, R., Qualitative and Quantitative Phytochemical Studies of Acanthus ilicifolius. *Res J Phytochem* 2014, 8 (3), 133-138.
24. Gurudeeban, S.; Ramanathan, T.; Satyavani, K., Antimicrobial and radical scavenging effects of alkaloid extracts from Rhizophora mucronata. *Pharm Chem J* 2015, 49 (1), 34-37.
25. Gurudeeban, S.; Kaliamurthi, S.; Sheik, H. S.; Thiruganasambandam, R., Molecular docking, isolation and biological evaluation of Rhizophora mucronata flavonoids as anti-nociceptive agents. *Biomed Prev Nutr* 2014, 4 (4), 555-560.
26. Selvaraj, G.; Kaliamurthi, S.; Thirugnasambandan R., Effect of Glycosin alkaloid from Rhizophora apiculata in non-insulin dependent diabetic rats and its mechanism of action: In vivo and in silico studies. *Phytomedicine* 2016, 23(6):632-40.
27. Rajamanickam, E.; Gurudeeban, S.; Satyavani, K.; Ramanathan, T., Chemopreventive effect of Acanthus ilicifolius extract on modulating antioxidants, lipid peroxidation and membrane bound enzymes in diethyl nitrosamine induced liver carcinogenesis. *Int J Cancer Res* 2016, 12 (1), 1-16.
28. Kaliamurthi, S.; Selvaraj, G.; Thirugnanasambandam, R.; Thangavel, B., Influence of rutoside loaded solid lipid nanoparticles to enhance oral bioavailability: characterization, pharmacokinetic, and pharmacodynamic studies. *Adv Sci, Eng Med* 2016, 8 (5), 350-359.
29. Kaliamurthi, S.; Selvaraj, G.; Thirugnanasambandam, R.; Thangavel, B., Topical Delivery of Nano-encapsulated Rutoside Medication for Diabetic Foot Ulcer in Rat Model. *Nanosci Nanotech Asia* 2018, 8 (1), 116-129.

30. Satyavani, K.; Gurudeeban, S.; Ramanathan T., Inhibitory effect of Excoecaria Agallocha L. Extracts on elastase and collagenase and identification of metabolites using HPLC-UV-MS techniques. *Pharm Chem J* 2018, 51(11):960-4.
31. Manigandan, V.; Gurudeeban, S.; Satyavani, K; Ramanathan, T., Molecular docking studies of Rhizophora mucronata alkaloids against neuroinflammatory marker cyclooxygenase 2. *Int J Biol Chem* 2014, 8: 91-99.
32. Gurudeeban, S.; Satyavani, K.; Ramanathan, T.; Ravikumar, P., Dipeptidyl peptidase IV inhibitors derived from a mangrove flora Rhizophora mucronata: An in silico approach. *Bangladesh J Pharmacol* 2012, 7(3):203-10.
33. Selvaraj, G.; Kaliamurthi, S.; Thirugnanasambandam, R., Molecular docking studies on potential PPAR-γ agonist from Rhizophora apiculata. *Bangladesh J Pharmacol* 2014, 9(3):298-302.
34. Gurudeeban, S.; Satyavani, K.; Ramanathan, T.; Balasubramanian, T., An in silico approach of alpha-ketoglutarate dependent dioxygenase FTO inhibitors derived from Rhizophora mucronata. *Drug Invention Today* 2012, 4(11): 594-598.
35. Dittrich, C.; Fridrik, M.A.; Koenigsberg, R.; Lee, C.; Goeldner, R.G.; Hilbert, J.; Greil, R. A phase 1 dose escalation study of BI 831266, an inhibitor of Aurora kinase B, in patients with advanced solid tumors. *Invest New Drugs.* 2015, 33(2):409-22. [CrossRef] [PubMed]
36. Cheung, C.H.; Sarvagalla, S.; Lee, J.Y.; Huang, Y.C.; Coumar, M.S. Aurora kinase inhibitor patents and agents in clinical testing: an update (2011 - 2013). *Expert Opin Ther Pat.* 2014, 24(9):1021-38. [CrossRef] [PubMed]
37. Yan, A.; Wang, L.; Xu, S.; Xu, J. Aurora-A kinase inhibitor scaffolds and binding modes. *Drug Discov Today*. 2011; 16(5-6):260-9. [CrossRef] [PubMed]
38. Srivastava, A.K.; Pandey, A.K.; Jain, S.; Misra, N. FT-IR spectroscopy, intra-molecular C-H···O interactions, HOMO, LUMO, MESP analysis and biological activity of two natural products, triclisine and rufescine: DFT and QTAIM approaches. *Spectrochim Acta A Mol Biomol Spectrosc.* 2015;136 Pt B:682-9. [CrossRef] [PubMed]
39. B, F.R.; Prasana, J.C.; Muthu, S.; Abraham, C.S. Molecular docking studies, charge transfer excitation and wave function analyses (ESP, ELF, LOL) on valacyclovir: A potential antiviral drug. *Comput Biol Chem.* 2019; 78:9-17. [CrossRef] [PubMed]
40. Kirubakaran, P.; Arunkumar, P.; Premkumar, K.; Muthusamy, K. Sighting of tankyrase inhibitors by structure- and ligand-based screening and in vitro approach. *Mol Biosyst.* 2014, 10(10):2699-712. [CrossRef] [PubMed]
41. Carry, J.C.; Clerc, F.; Minoux, H.; Schio, L.; Mauger, J.; Nair, A.; Parmantier, E.; Le Moigne, R.; Delorme, C.; Nicolas, J.P.; Krick, A.; Abécassis, P.Y.; Crocq-Stuerga, V.; Pouzieux, S.; Delarbre, L.; Maignan, S.; Bertrand, T.; Bjergarde, K.; Ma, N.; Lachaud, S.; Guizani, H.; Lebel, R.; Doerflinger, G.; Monget, S.; Perron, S.; Gasse, F. Angouillant-Boniface O, Filoche-Rommé B, Murer M, Gontier S, Prévost C, Monteiro ML, Combeau C. SAR156497, an exquisitely selective inhibitor of aurora kinases. *J Med Chem.* 2015, 8;58(1):362-75. [CrossRef] [PubMed]
42. Fancelli D, Berta D, Bindi S, Cameron A, Cappella P, Carpinelli P, Catana C, Forte B,

Giordano P, Giorgini, M.L.; Mantegani, S.; Marsiglio, A.; Meroni, M.; Moll, J.; Pittalà, V.; Roletto, F.; Severino, D.; Soncini, C.; Storici, P.; Tonani, R.; Varasi, M.; Vulpetti, A.; Vianello, P. Potent and selective Aurora inhibitors identified by the expansion of a novel scaffold for protein kinase inhibition. *J Med Chem.* 2005; 48(8):3080-4. [CrossRef] [PubMed]

43. Chang, J.H.; Lai, S.L.; Chen, W.S.; Hung, W.Y.; Chow, J.M.; Hsiao, M.; Lee, W.J.; Chien, M.H.; Quercetin suppresses the metastatic ability of lung cancer through inhibiting Snail-dependent Akt activation and Snail-independent ADAM9 expression pathways. *Biochim Biophys Acta Mol Cell Res.* 2017,1864(10):1746-1758. [CrossRef] [PubMed]
44. Boadi, W.Y.; Lo. A. Effects of Quercetin, Kaempferol, and Exogenous Glutathione on Phospho- and Total-AKT in 3T3-L1 Preadipocytes. *J Diet Suppl.* 2018, 2;15(6):814-826. [CrossRef] [PubMed]
45. Wu, T.C.; Chan, S.T.; Chang, C.N.; Yu, P.S.; Chuang, C.H.; Yeh, S.L. Quercetin and chrysin inhibit nickel-induced invasion and migration by downregulation of TLR4/NF-κB signaling in A549 cells. *Chem Biol Interact.* 2018, 25;292:101-109. [CrossRef] [PubMed]
46. Liu, H.; Zhou, M. Antitumor effect of Quercetin on Y79 retinoblastoma cells via activation of JNK and p38 MAPK pathways. *BMC Complement Altern Med.* 2017, 13;17(1):531. [CrossRef] [PubMed]
47. Xingyu, Z.; Peijie, M.; Dan, P.; Youg, W.; Daojun, W.; Xinzheng, C.; Xijun, Z.; Yangrong, S. Quercetin suppresses lung cancer growth by targeting Aurora B kinase. *Cancer Med.* 2016, 5(11):3156-3165. [CrossRef] [PubMed]
48. Hung, T.W.; Chen, P.N.; Wu, H.C.; Wu, S.W; Tsai, P.Y.; Hsieh, Y.S.; Chang, H.R. Kaempferol Inhibits the Invasion and Migration of Renal Cancer Cells through the Downregulation of AKT and FAK Pathways. *Int J Med Sci.* 2017, 18;14(10):984-993. [CrossRef] [PubMed]
49. Han, X.; Liu, C.F.; Gao, N.; Zhao, J.; Xu, J. Kaempferol suppresses proliferation but increases apoptosis and autophagy by up-regulating microRNA-340 in human lung cancer cells. *Biomed Pharmacother.* 2018,108:809-816. [CrossRef] [PubMed]
50. Pham, H.N.T.; Sakoff, J.A.; Vuong, Q.V.; Bowyer, M.C.; Scarlett, C.J. Comparative cytotoxic activity between kaempferol and gallic acid against various cancer cell lines. *Data Brief.* 2018, 27;21:1033-1036. [CrossRef] [PubMed]
51. Jeong, H.; Phan, A.N.H.; Choi, J.W. Anti-cancer Effects of Polyphenolic Compounds in Epidermal Growth Factor Receptor Tyrosine Kinase Inhibitor-resistant Non-small Cell Lung Cancer. *Pharmacogn Mag.* 2017, 13(52):595-599. [CrossRef] [PubMed]
52. Liao, W.; Chen, L.; Ma, X.; Jiao, R.; Li, X.; Wang, Y. Protective effects of kaempferol against reactive oxygen species-induced hemolysis and its antiproliferative activity on human cancer cells. *Eur J Med Chem.* 2016, 23;114:24-32. [CrossRef] [PubMed]
53. Jiang, Z.Q.; Li, M.H.; Qin, Y.M.; Jiang, H.Y.; Zhang, X.; Wu, M.H. Luteolin Inhibits Tumorigenesis and Induces Apoptosis of Non-Small Cell Lung Cancer Cells via Regulation of MicroRNA-34a-5p. *Int J Mol Sci.* 2018, 2;19(2). pii: E447. [CrossRef] [PubMed]
54. Lee, Y.J.; Lim, T.; Han, M.S.; Lee, S.H.; Baek, S.H.; Nan, H.Y.; Lee, C. Anticancer effect of luteolin is mediated by downregulation of TAM receptor tyrosine kinases, but not interleukin-8, in non-small cell lung cancer cells. *Oncol Rep.* 2017, 37(2):1219-1226. [CrossRef] [PubMed]

55. Wang, Y.; Zhang, Y.; Chen, X.; Hong, Y.; Wu, Z. [Combined treatment with myo-inositol and luteolin selectively suppresses growth of human lung cancer A549 cells possibly by suppressing activation of PDK1 and Akt]. *Nan Fang Yi Ke Da Xue Xue Bao.* 2018, 30;38(11):1378-1383. [CrossRef] [PubMed]
56. Sonoki, H.; Tanimae, A.; Endo, S.; Matsunaga, T.; Furuta, T.; Ichihara, K.; Ikari, A. Kaempherol and Luteolin Decrease Claudin-2 Expression Mediated by Inhibition of STAT3 in Lung Adenocarcinoma A549 Cells. *Nutrients.* 2017, 13;9(6). [CrossRef] [PubMed]
57. Zhou, M.; Shen, S.; Zhao, X.; Gong, X. Luteoloside induces G(0)/G(1) arrest and pro-death autophagy through the ROS-mediated AKT/mTOR/p70S6K signalling pathway in human non-small cell lung cancer cell lines. *Biochem Biophys Res Commun.* 2017, 9;494(1-2):263-269. [CrossRef] [PubMed]
58. Hosseinzadeh, H.; Nassiri-Asl, M. Review of the protective effects of rutin on the metabolic function as an important dietary flavonoid. *J Endocrinol Invest.* 2014, 37(9):783-8. [CrossRef] [PubMed]
59. Araújo, J.R.; Gonçalves, P.; Martel, F. Chemopreventive effect of dietary polyphenols in colorectal cancer cell lines. *Nutr Res.* 2011, 31(2):77-87. [CrossRef] [PubMed]
60. Wu, F.; Chen, J.; Fan, L.M.; Liu, K.; Zhang, N.; Li, S.W.; Zhu, H.; Gao, H.C. Analysis of the effect of rutin on GSK-3β and TNF-α expression in lung cancer. *Exp Ther Med.* 2017, 14(1):127-130. doi: 10.3892/etm.2017.4494. [CrossRef] [PubMed]
61. Shahid, A.; Ali, R.; Ali, N.; Hasan, S.K.; Rashid, S.; Majed, F.; Sultana, S. Attenuation of genotoxicity, oxidative stress, apoptosis and inflammation by rutin in benzo(a)pyrene exposed lungs of mice: plausible role of NF-κB, TNF-α and Bcl-2. *J Complement Integr Med.* 2016 Mar;13(1):17-29. [CrossRef] [PubMed]
62. Ben Sghaier, M.; Pagano, A.; Mousslim, M.; Ammari, Y.; Kovacic, H.; Luis, J. Rutin inhibits proliferation, attenuates superoxide production and decreases adhesion and migration of human cancerous cells. *Biomed Pharmacother.* 2016, 84:1972-1978. [CrossRef] [PubMed]
63. Becke A.D. A new mixing of Hartree–Fock and local density-functional theories. *J Chem Phys.*, **1993,** *98* (2), 1372-1377, DOI.org/10.1063/1.464304. [CrossRef] [PubMed]
64. Khokhar, S.; Feng, Y.; Campitelli, M.R.; Quinn, R.J.; Hooper, J.N.; Ekins, M.G.; Davis R.A. Trikentramides A-D, indole alkaloids from the Australian sponge Trikentrion flabelliforme. *J Nat Prod.* 2013, 22;76(11):2100-5. [CrossRef] [PubMed]
65. Lee, C.; Yang, W.; Paar, R.G. Development of the Colle-Salvetti correlation-energy formula in to a functional of the electron density. *Journal of Physics Condensed Matter*, 1998; 37, 785–789.
66. Muthusamy, K.; Chinnasamy, S.; Nagarajan, S.; Sivaraman, T.; Chinnasamy, S. Isolation and characterization of bioactive compounds of Clematis gouriana Roxb. ex DC against snake venom phospholipase A(2) (PLA(2)) computational and in vitro insights. *J Biomol Struct Dyn.* 2017 Jul;35(9):1936-1949. [CrossRef] [PubMed]
67. Pietro, W.J.; Francl, M.M.; Hehre, W.J.; DeFrees, D.J.; Pople, J.A.; Binkley, J.S. Self-consistent molecular orbital methods. 24. Supplemented small split-valence basis sets for second-row elements. *J Am Chem Soc.* 1982; 104, 5039–5048. [CrossRef] [PubMed]
68. Cho, A.E.; Guallar, V.; Berne, B.J.; Friesner, R. Importance of Accurate Charges in Molecular Docking: Quantum Mechanical/Molecular Mechanical (QM/MM) Approach. *J Comput Chem*

**2005,** *26* (9), 915-931. [CrossRef] [PubMed]

69. Naik, P.K.; Santoshi, S.; Rai, A.; Joshi, H.C. Molecular modelling and competition binding study of Br-noscapine and colchicine provide insight into noscapinoid-tubulin binding site. *J Mol Graph Model.* 2011, 29(7):947-55. [CrossRef] [PubMed]
70. Chinnasamy, S.; Nagamani, S.; Muthusamy, K. $Zn^{2+}$ ion of the snake venom metalloproteinase (SVMP) plays a critical role in ligand binding: a molecular dynamics simulation study. *RSC Adv.* 2015, 5, 70566. [CrossRef]
71. Hess, B.; Kutzn Portella er, C.; van der Spoel, D.; Lindahl, E. GROMACS 4: Algorithms for Highly Efficient, Load-Balanced, and Scalable Molecular Simulation. *J Chem Theory Comput.* 2008, 4(3):435-47. [CrossRef] [PubMed]
72. Muthusamy, K.; Chinnasamy, S.; Nagarajan, S.; Sivaraman, T.; Chinnasamy, S. Isolation and characterization of bioactive compounds of Clematis gouriana Roxb. ex DC against snake venom phospholipase A(2) (PLA(2)) computational and in vitro insights. *J Biomol Struct Dyn.* 2017 Jul;35(9):1936-1949. [CrossRef] [PubMed]
73. Ali, M.; Pandey, R.K.; Khatoon, N.; Narula, A.; Mishra, A.; Prajapati, V.K.; Exploring dengue genome to construct a multi-epitope-based subunit vaccine by utilizing immunoinformatics approach to battle against dengue infection. *Sci Rep.* 2017, 23;7(1):9232. [CrossRef] [PubMed]
74. SchuÈttelkopf, A.W.; Van Aalten, D.M. PRODRG: a tool for high-throughput crystallography of protein–ligand complexes. *Acta Crystallographica Section D: Biological Crystallography* 2004; 60, 1355-1363. [CrossRef] [PubMed]
75. Canzar, S.; El-Kebir, M.; Pool, R.; Elbassioni, K.; Malde, A.K.; Mark, A.E.; Geerke, D.P.; Stougie, L.; Klau, G.W. Charge group partitioning in biomolecular simulation. *J Comput Biol.* 2013:188-98. [CrossRef] [PubMed]
76. Malde, A.K.; Zuo, L.; Breeze, M.; Stroe,t M.; Poger, D.; Nair P.C.; Oostenbrink, C.; Mark, A.E. An Automated Force Field Topology Builder (ATB) and Repository: Version 1.0. *J Chem Theory Comput.* 2011, 13;7(12):4026-37. [CrossRef] [PubMed]
77. Yahyaei, M.; Mehrnejad, F.; Naderi-Manesh, H.; Rezayan, A.H. Follicle-stimulating hormone encapsulation in the cholesterol-modified chitosan nanoparticles via molecular dynamics simulations and binding free energy calculations. *Eur J Pharm Sci.* 2017; 30; 107:126-137.
78. Payne, M.; Teter, M.P.D.; Allan, D.C.; Arias, T.A.; Joannopoulos, J.D. Iterative minimization techniques for ab initio total-energy calculations: Molecular dynamics and conjugate gradients. *Rev Mod Phys.* 1992; 64, 1045–1097. [CrossRef] [PubMed]
79. Darden, T.; York, D.; Pedersen, L. Particle mesh Ewald: An N· log (N) method for Ewald sums in large systems. *J Chem Phys.* 1993, *98* (12), 10089-10092. [CrossRef] [PubMed]